J Opt
https://doi.org/10.1007/s12596-022-00962-5

RESEARCH ARTICLE

Full-space metasurface in mid-infrared based on phase change material of VO_2

Xueqiang Fan[1] · Qianlong Kang[1] · Huifang Ai[1] · Kai Guo[1] · Zhongyi Guo[1]

Received: 28 June 2022 / Accepted: 30 August 2022

Abstract Most of the traditional metasurfaces are passive and work with a single function, which limits their application in integrated devices. Phase change materials based metasurfaces offer flexible functions. In this work, we proposed a full-space tunable metasurface working at wavelength of 8.5 μm based on vanadium dioxide (VO_2). When the VO_2 is metallic, the metasurface works as a half-wave plate in reflective mode and the polarization conversion efficiency through the metasurface could be greater than 90% over a broadband range of 1.32 μm. When the VO_2 is insulated, the metasurface works as a focusing lens in transmission mode with focusing efficiency up to 65% and full-width half-maximum (FWHM) of 0.67 λ. This result may provide a new route for the development of multifunctional devices.

Keywords metasurface · vanadium dioxide · full-space · mid-infrared

Introduction

Metasurface can be regarded as a two-dimensional counterpart of metamaterial with subwavelength thickness [1–4]. Compared with three-dimensional metamaterials, metasurfaces have unique advantages in manufacturing and integration [5–8]. Metasurfaces can achieve flexible and effective modulation of electromagnetic wave, such as amplitude, phase, and polarization [9–13]. In recent years, new optical phenomena and devices based on metasurfaces have been realized, such as anomalous refraction and reflection [14–17], focusing lenses [18, 19], perfect absorbers [20, 21] and holography [22–24]. However, most previous designs are passive, which means that the metasurface has a fixed function. From a practical point of view, it would be beneficial if metasurface based devices could have multiple functions [25–28].

Multifunctional metasurfaces are usually achieved by integrating metasurfaces with different functions into a same layer or by stacking them in different layers [29]. A number of metasurfaces for full-space electromagnetic wave manipulation via cascaded structure of multilayer media have been reported [30–34]. Another effective approach is to build metasurfaces with tunable materials such as graphene, indium tin oxide (ITO) and phase change materials, obtaining new degrees of freedom for electromagnetic field manipulation [35–37]. Vanadium dioxide (VO_2) is a typical reversible phase change material, which is insulated at room temperature and turns into metallic state when the temperature reaches ~ 341 K [38]. Recently, more and more researchers have tried to achieve tunable metasurfaces with VO_2 [39–43]. In 2018, Ding et al. studied the VO_2 metasurface and demonstrated that it could be switched between an absorber and a half-wave plate at the terahertz frequency as the VO_2 undergoes phase transition [44]. In 2019, Chen et al. proposed a spin-dependent switchable metasurface working at $\lambda = 4.55$ μm that achieves focusing and absorbing functions by introducing a very thin VO_2 film [45]. In 2021, Kang et al. achieved tunable wavefront and polarization manipulation of terahertz wave by using metasurface based on VO_2 dipole antennas [46]. Nevertheless, full-space tunable metasurface working in the mid-infrared region still remains an interesting task.

✉ Kai Guo
kai.guo@hfut.edu.cn

Zhongyi Guo
guozhongyi@hfut.edu.cn

[1] School of Computer and Information, Hefei University of Technology, Hefei 230601, China

Published online: 13 September 2022

In this work, we design a full-space metasurface working at wavelength of 8.5 μm based on the metal–insulator transition properties of VO_2. The designed metasurface allows control both the transmitted and reflected fields. As a proof of concept, we numerically simulated the metasurface that works as a focusing lens and half-wave plate with insulated and metallic VO_2, respectively. The focusing efficiency and polarization conversion efficiency are investigated. We also study the broadband performance of the half-wave plate. In addition, we investigate performance of the metasurface when VO_2 is at the intermediated state, demonstrating the metasurface could work in both transmission and reflection sides simultaneously, i.e., full-space metasurface. Our work provides new ideas for the realization of full-space multifunctional devices, which will have a wide range of applications in electromagnetically integrated systems.

Results and discussion

Our schematic diagram of the designed metasurface structure is shown in Fig. 1, cascading two functional metasurfaces. Figure 1a shows the function of the designed metasurface, focusing in transmission mode and polarization conversion in reflection mode. In reflection mode, the designed structure could be treated as a metal–insulator-metal configuration, as shown in Fig. 1b. The top layer is VO_2 antennas with tilted angle of 45°, the middle layer is CaF_2, and the bottom layer is a VO_2 thin film layer. In transmission mode, the VO_2 is insulator and the designed structure could be treated as in Fig. 1c, i.e., the unit element consists of silicon columns located on CaF_2 substrate. The unit period is $p = 2.5$ μm. The height, length, and width of VO_2 antenna is $t_4 = 0.4$ μm, $L = 2.4$ μm, and $W = 0.9$ μm, respectively. The thickness of VO_2 film sandwiched by CaF_2 is $t_2 = 0.4$ μm, the thicknesses of the two CaF_2 layers are $t_1 = 1$ μm and $t_3 = 0.7$ μm. The height of the silicon column is $h = 6.5$ μm, and the radius r varies according to the requirement of phase modulation of transmission. When VO_2 is heated, it transitions from insulated to metallic states, resulting in the metasurface switching from transmission to reflection modes, and vice versa.

A home-made program based on the finite element method is used to perform numerical simulations. A plane wave with x-polarization and wavelength of 8.5 μm is perpendicularly incident to the metasurface along the z-direction. Periodic boundary conditions are used in the x- and y-directions, and perfectly matched layers are used in the z-direction. For simplicity, the optical responses of Si and CaF_2 are described by loss-free refractive indices of $n = 3.42$ and $n = 1.4$, respectively. At mid-infrared range, the dielectric constant for VO_2 is calculated using the simple Looyenga rule [47]:

$$\varepsilon_{eff}^{s} = (1-f)\varepsilon_{i}^{s} + f\varepsilon_{m}^{s} \quad (1)$$

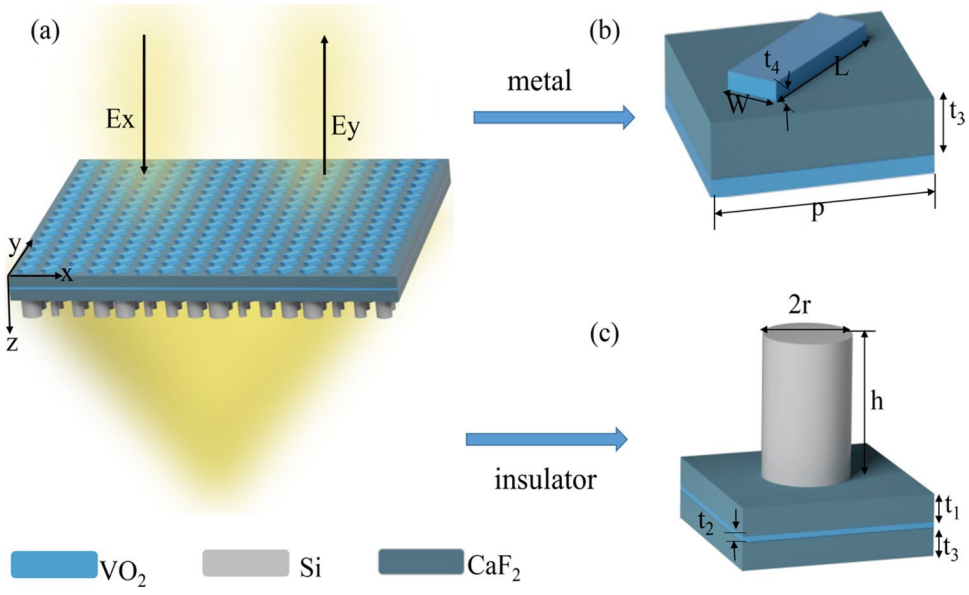

Fig.1 Three-dimensional schematic of the metasurface structure. **a** Schematic diagram of a full-space tunable multifunctional metasurface, a unit cell at the **b** front side and **c** back side. When VO_2 is in metallic state, the metasurface works in reflective mode. When VO_2 is in insulator phase, the metasurface works in transmissive mode

where ε_{eff} is the complex permittivity of VO_2, f is the temperature dependent volume fraction of the metallic VO_2, ε_i and ε_m are the complex dielectric constants of the insulated and metallic VO_2, respectively. $\varepsilon_i = (2.45 + i \bullet 0.07)^2$ and $\varepsilon_m = (6.55 + i \bullet 9.8)^2$ at wavelength of 8.5 μm [47]. s is related to the shape of the metal inclusions and values between -1 and 1, herein we set $s = 0.3$ [48]. In addition, the volume fraction f as a function of temperature T can be described by the Boltzmann function [49, 50]:

$$f(T) = f \frac{1}{1 + \exp[(T - T_0)/\Delta T]_{max}} \quad (2)$$

where f_{max} is the maximum volume fraction of VO_2 in metal phase at the highest temperature, T_0 is the phase change temperature, for heating and cooling process, $T_0 = 68$ °C and $T_0 = 64$ °C, respectively, ΔT is the transition width. According to the experimental results in [50], $\Delta T = 2$ °C and $f_{max} = 0.95$. In simple words, the metal volume fraction of VO_2 can be controlled by tuning temperature, resulting in tunable optical responses.

The mechanism for the different functions in the insulating and metallic states is mainly the different principles of implementation. In the metallic state, the metal–insulator-metal (MIM) structure of the metasurface is approximated as a Fabry–Perot resonator, which usually comprises two parallel plates [51]. Figure 2a is the structure electric field diagram in the metal state. It can be clearly seen that the electric field is mainly concentrated in the MIM structure, which is consistent with the designed reflective function. As shown in Fig. 2b, the efficient broadband polarization transition of our designed metasurface can be further explained by the theory of multiple interferences. In the MIM cavity, multiple reflections of cross-polarization interfere constructively, while multiple reflections of co-polarization interfere destructively, increasing the performance of cross-polarization [52]. When the metasurface is at room temperature, VO_2 is an insulating state, and it is a dielectric metasurface. In the transmission mode, the silicon column can be regarded as a cavity supporting waveguide-like cavity resonances, which can achieve 2π phase coverage by changing the effective refractive index of the silicon column (i.e., the radius of the column), while maintaining high transmittance. The implementation of 2 π phase makes it possible to design many functions. Figure 2c is the electric field diagram in the silicon column. It is noteworthy that we chose a relatively high height of nanoblocks $h = 6.5$ μm. Therefore, multiple resonances can be excited inside the silicon nanoblocks to obtain a larger phase compensation. Figure 2d is the schematic diagram of transmission, in which the VO_2 is insulator and the incident light is transmitted. The

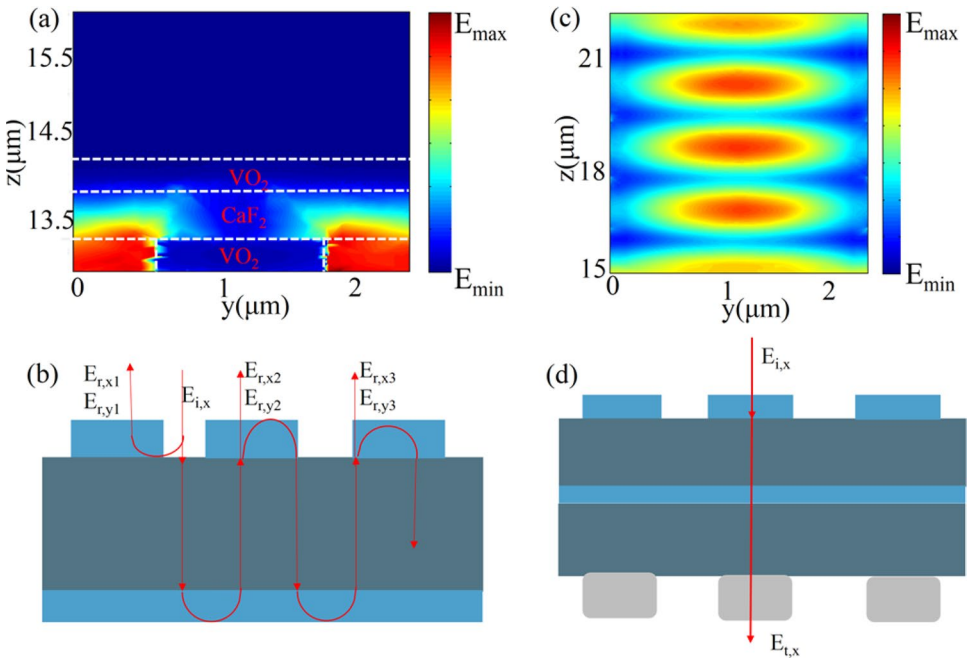

Fig. 2 **a** The electric field distribution in reflection mode. **b** Schematic of multiple reflections in the Fabry–Perot-like metasurface polarization converter in reflection. **c** Electric field distribution in transmission mode. **d** Schematic diagram of transmission

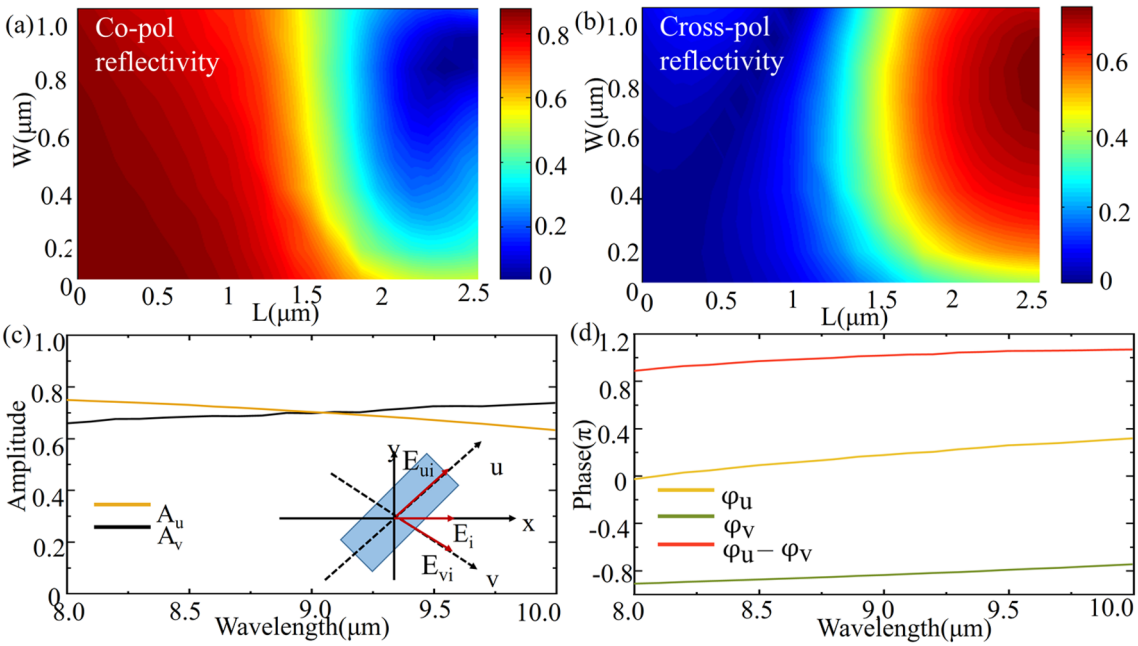

Fig. 3 **a** Co-polarization and **b** cross-polarization reflectivity as functions of the length (L) and width (W) of the VO_2 antenna at working wavelength of 8.5 μm. **c** The amplitudes of reflection along u and v directions when x-polarized light is incident. **d** The reflected phase and relative phase difference of x-polarization light along the u and v axes

silicon nanoblocks at the bottom provides the abrupt phase to modulate the wavefront of the incident light.

When VO_2 is heated to its metallic state, the metasurface works in reflection mode, and the metasurface structure is approximately an MIM structure. The unit structure is shown in Fig. 3c. Firstly, simulations of structural cells were carried out to investigate the metasurface reflection when x-polarization light at an operating wavelength of 8.5 μm is incident vertically. Figure 3a, b shows the dependence of the co-polarization and cross-polarization, respectively, on the values of length (L) and width (W) of the VO_2 antenna. It can be seen that when the period (P) of the cell structure is constant, the higher the values of L and W, the more x-polarization will be converted into y-polarization. Herein we set $L = 2.4$ μm and $W = 0.9$ μm to avoid structural intersection and coupling between neighboring elements. Figure 3c plots the amplitudes of reflection along u and v directions (see the inset) as functions of incident wavelength, which is x-polarized and vertically incident along z-direction. Due to obliquely oriented VO_2 antenna with angle of 45°, the incident wave and the excited electric field could be decomposed into the u and v components. Figure 3 d shows the variation in reflection phase as the wavelength is varied from 8.0 μm to 10.0 μm with fixed L and W. It can be seen that the reflection amplitudes are approximately equal and greater than 60% in the operating wavelength range, and the difference in phase between the reflected fields along u and v axis is close to π. It means that polarization direction of the reflected wave will rotate an angle of $\pi/2$, and cross-polarized wave is generated in the working wavelength range.

Jones matrix may help us to understand the above polarization conversion. Assuming a metasurface lying in the x–y plane, we can first define it as having a Jones matrix of general form:

$$\mathrm{J} = \begin{pmatrix} J_{xx} & J_{xy} \\ J_{yx} & J_{yy} \end{pmatrix} \tag{3}$$

where J_{xx} and J_{xy} represent the transmission coefficient with x- and y-polarization, respectively, under x-polarized incidence, and J_{yy} and J_{yx} represent the transmission coefficient with y- and x-polarization, respectively, under y-polarized incidence. There is basically no coupling between x and y polarizations, i.e., $J_{xy} = J_{yx} = 0$. When a polarized light is incident, for the metasurface structure with a titled angle θ between the optical axis and the x axis, as shown in Fig. 3(c), its transmission matrix in the Cartesian coordinate system is:

$$J^* = R(-\theta)\begin{pmatrix} J_{xx} & J_{xy} \\ J_{yx} & J_{yy} \end{pmatrix}R(\theta) = \begin{pmatrix} J_{xx}\cos^2\theta + J_{yy}\sin^2\theta - \frac{1}{2}(J_{xy}+J_{yx})\sin 2\theta & J_{xy}\cos^2\theta - J_{yx}\sin^2\theta + \frac{1}{2}(J_{xx}-J_{yy})\sin 2\theta \\ J_{yx}\cos^2\theta - J_{xy}\sin^2\theta + \frac{1}{2}(J_{xx}-J_{yy})\sin 2\theta & J_{yy}\cos^2\theta + J_{xx}\sin^2\theta + \frac{1}{2}(J_{xy}+J_{yx})\sin 2\theta \end{pmatrix} \quad (4)$$

where $\mathbf{R}(\theta) = [\cos\theta, \sin\theta; -\sin\theta, \cos\theta]$ is the standard second-order rotation matrix. When incident light is *x*-polarized $\mathbf{E}_{in} = \begin{bmatrix} 1 & 0 \end{bmatrix}^T$, its outgoing light can be expressed as:

$$\mathbf{E}_{out} = \mathbf{J}^*\mathbf{E}_{in} = \begin{bmatrix} J_{xx}\cos^2\theta + J_{yy}\sin^2\theta \\ (J_{yy} - J_{xx})sin\theta\cos\theta \end{bmatrix} \quad (5)$$

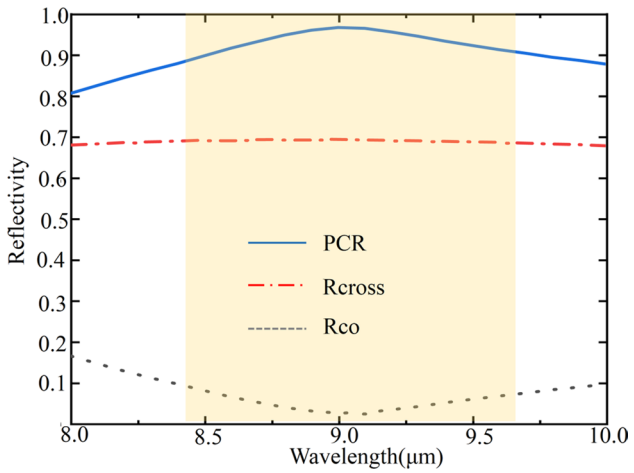

Fig. 4 When the designed structure works in reflection mode, the reflectance of co-polarization and cross-polarization light, and the PCR

The rotation angle of the antenna is $\theta = 45°$, the phase delay between the long and short axes of the antenna is π. As the amplitude is almost same in each direction, $J_{xx} = -J_{yy}$, then we have the output light $\mathbf{E}_{out} = \begin{bmatrix} 0 & 1 \end{bmatrix}^T$ and it is *y*-polarized. At this time, the cross-polarization conversion is completed, and the linear polarization conversion efficiency reaches the maximum.

According to the above analysis, we can design and achieve the function of half-wave plate in reflection mode. When the metasurface structure is heated using a femtosecond laser, VO_2 will be in the metallic state. As can be seen from Fig. 1a, since the continuous VO_2 film becomes metallic and the metasurface structure can be simplified as Fig. 1b. Here the incident light is *x*-polarized, thus the co-polarization reflectivity is defined as $|r_{co}|^2 = |E_{xr}/E_i|^2$, and the cross-polarization reflectivity is defined as $|r_{cr}|^2 = |E_{yr}/E_i|^2$, where E_{xr} and E_{yr} are the reflection of x-polarization and y-polarization, respectively. To investigate, the polarization conversion ratio (PCR) is defined as $PCR = R_{cr}/(R_{co} + R_{cr})$, where R_{cr} and R_{co} are the reflection of cross- and co-polarization, respectively, equal to $|r_{co}|^2$ and $|r_{cr}|^2$, respectively. Figure 4 shows the value of PCR in the wavelength range of 8.0 μm–10 μm. As can be seen, the cross-polarization conversion rate is above 68% in the range from 8.4 μm to 9.72 μm, while the co-polarization conversion rate is below 10%. The PCR can be obtained above 90%, indicating the great performance

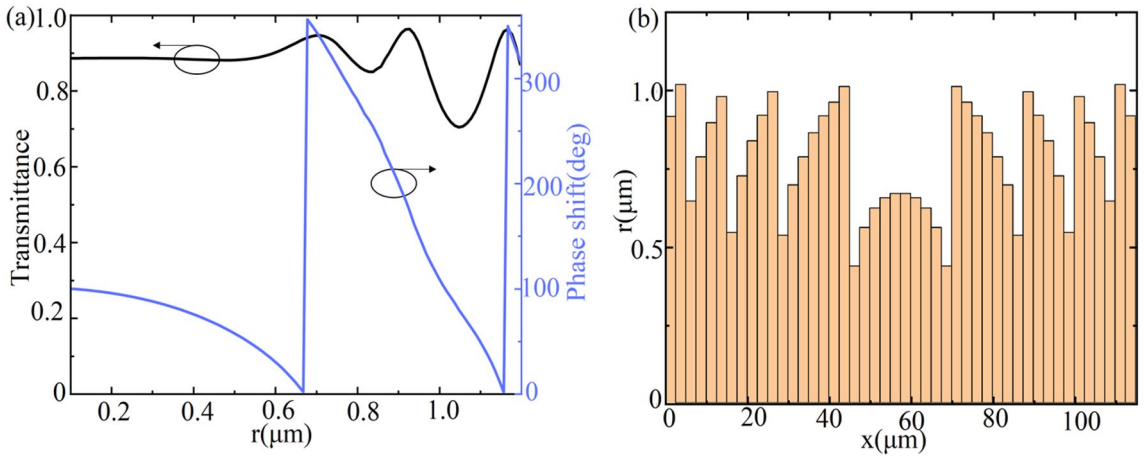

Fig. 5 **a** Transmission phase and transmittance for silicon cylindrical radius from r = 0.1 μm to r = 1.2 μm. **b** The radius(r) distribution for focusing x-polarization at a focal length of 38 μm with an operating wavelength of 8.5 μm

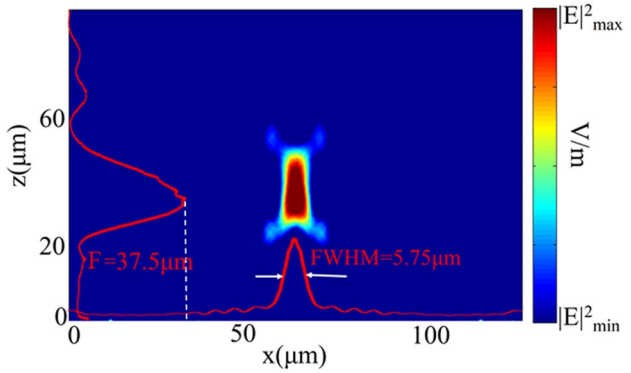

Fig. 6 When the designed structure works in transmission mode, the metasurface is designed to operate at 8.5 μm with a focal length of $F = 38$ μm. Simulation of the electric field intensity distribution of a meta-len focused in the x–z plane. The red lines in the figures demonstrate the concrete profiles of the FMWHs and focal length along the x- and z-directions

of polarization conversion. Due to the specific symmetry and working principles, the designed structure may work well for circularly polarized light by optimizing the geometry parameters.

To demonstrate that our designed metasurface can also work in transmission mode, a focusing lens is designed. The phase and amplitude of the transmitted light are shown in Fig. 5a as functions of the radius r of the silicon column. It can be seen that the phase of the transmitted light can reach a phase coverage of 0-2 π when the silicon column radius is varied from 0.1 μm to 1.2 μm, and the transmittance is above 75%, ensuring that the metasurface could artificially engineer the wavefront of transmitted light.

The phase distribution of the focusing metasurface along x axis can be calculated by:

$$\varphi(x) = -2\pi/\lambda \cdot \left(\sqrt{(x - x_0)^2 + F^2} - F\right) \tag{6}$$

where λ is the incident wave length, (x_0, F) are the coordinates of any focal point of our design, and F is the focal length of the design. When the designed phase profile satisfies Eq. 6, the incident plane wave will converge to a spherical wave and achieve the focusing function. Based on the desired phase profile and the results in Fig. 5a, we can easily determine the radius of the silicon column at each position. Figure 5b shows the value of required radius r distribution for the designed focusing metasurface, which operates at wavelength of 8.5 μm and the focal length is $F = 38$ μm.

Figure 6 shows the simulated focused electric field distribution of the focusing metasurface in the x–z plane at wavelength of 8.5 μm. The symmetry of silicon cylinders allows polarization insensitive properties, therefore x-polarized incident light is used to verify the focusing performance. It is clear that a strong focus exists at a distance of approximately 38 μm from the structure, which is consistent with the designed value. The focusing efficiency of the metasurface is defined as the ratio of the focus energy to the incident energy and calculated as 65%.

In order to further investigate the focusing performance, we investigated more quantities characterizing the focusing effect of lenses. The first quantity is the numerical aperture (NA), calculated by $NA = \sin[\tan^{-1}(D/2F)]$, where D represents the total width of the metasurface and F is the focal length. Generally, the larger the numerical aperture, the better the focusing effect of a lens. The value of NA of the designed metasurface is calculated to be 0.834, demonstrating the good ability of focusing. The red lines in the figures along z-direction shows that the focal length of the simulated metasurface is 37.5 μm. The

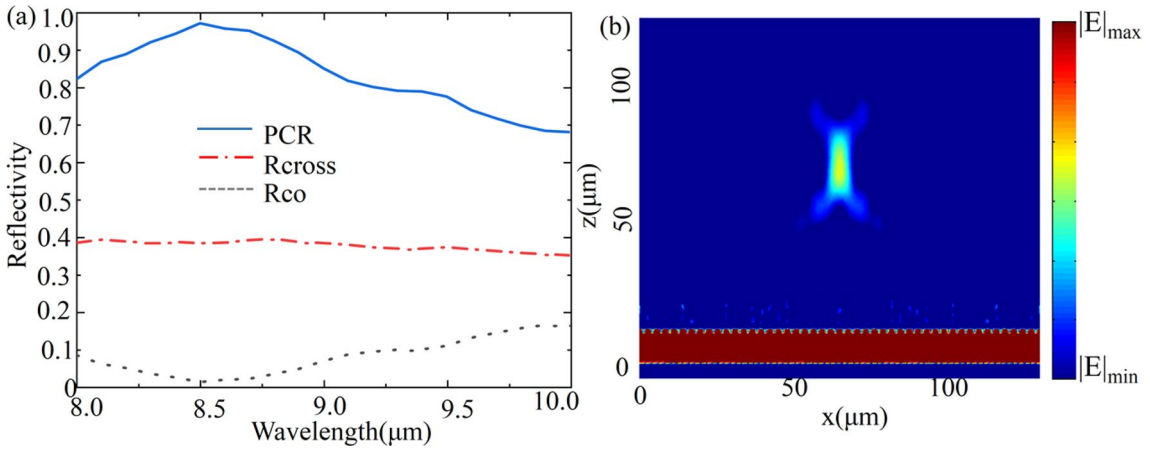

Fig. 7 When VO_2 is in the intermediate state ($f = 0.5$), the metasurface operates simultaneously as a half-wave plate and a focusing lens. **a** The reflectivity of co-polarization and cross-polarization, and the PCR. **b** The electric field intensity distribution of the focusing meta-len in the x–z plane

deviation of the simulated result from the designed value could be attributed to structural size constraints and phase deviation. The second quantity is the full width at half maximum (FWHM). Generally, the smaller the FWHM, the more energy at the focal point and the better the focusing effect. The red lines in the figures along x-direction shows that the FWHM of the designed metasurface is 5.76 μm (0.67 λ). These results demonstrate the excellent focusing performance of the designed metasurface.

It has been demonstrated that two distinct functions of transmission and reflection could be well achieved when VO_2 is insulated ($f=0$) and metallic ($f=1$), respectively. Owing to the continuously tunable characteristic of VO_2, it is necessary to investigate the performance of the designed metasurface in the intermediate state of VO_2. To this end, we simulated the metasurface when the crystalline fraction of VO_2 is $f=0.5$, as shown in Fig. 7. In this case, the metasurface can simultaneously obtain polarization conversion in reflection and focusing meta-lens in transmission. Figure 7a shows that the value of PCR is reduced compared to that when VO_2 is in metallic state (Fig. 4). It is due to that partial part of lights reflected back. Figure 7b shows the focusing effect of reflection. Compared to the insulated state (Fig. 6), the FWHM and focal length are almost unchanged, and the focusing intensity becomes weaker. It is because the focusing phase is provided by the silicon column. These results indicate that the ratio of transmission and reflection could be well manipulated by controlling the crystalline fraction of VO_2.

Conclusion

In conclusion, we have designed a full-space metasurface that can operate independently in both transmission and reflective modes, which improves space utilization. By controlling the temperature of VO_2 the designed metasurface, reversible switching between transmission mode and reflection mode have been realized. In the transmission mode, by controlling the radius of the silicon cylinder, a high transmittance with phase coverage from 0 to 2 π can be achieved, making it possible to artificially engineer the wavefront of transmission. We have designed a focusing metasurface at wavelength of 8.5 μm with a focusing efficiency of 65%. In the reflection mode, by placing the VO_2 antenna in the metallic state at a 45° angle to the x axis, the long and short axes create a relative phase difference of π, enabling the half-wave plate function. The polarization conversion is above 90% over a broadband wavelength from 8.4 μm to 9.72 μm. The simulation results have demonstrated that the designed metasurface has good focusing performance and polarization conversion capability in the mid-infrared band. The design of tunable metasurface with phase change materials provides an extra degree of freedom in the phase and wavefront control of the metasurface, which has a promising application in the design of integrated multifunctional devices.

Funding Natural Science Foundation of China (NSFC) (61775050, 11804073).

Data availability Data underlying the results presented in this paper are not publicly available at this time but may be obtained from the authors upon reasonable request.

Declarations

Conflict of interest The authors declare no conflicts of interest.

References

1. A.K. Iyer, A. Alu, A. Epstein, Metamaterials and metasurfaces-historical context, recent advances, and future directions. IEEE T. Antenn. Propag. **68**(3), 1223–1231 (2020)
2. A. Ali, A. Mitra, B. Aïssa, Metamaterials and metasurfaces: A review from the perspectives of materials, mechanisms and advanced metadevices. Nanomaterials **12**(6), 1027 (2022)
3. S.S. Bukhari, J. Vardaxoglou, W. Whittow, A metasurfaces review: Definitions and applications. Appl. Sci. **9**(13), 2727 (2019)
4. M. Kadic, G.W. Milton, M. van Hecke, M. Wegener, 3D metamaterials. Nat. Rev. Phys. **1**(3), 198–210 (2019)
5. N. Yu, F. Capasso, Flat optics with designer metasurfaces. Nat. Mater. **13**(2), 139–150 (2014)
6. S.M. Kamali, E. Arbabi, A. Arbabi, A. Faraon, A review of dielectric optical metasurfaces for wavefront control. Nanophotonics **7**(6), 1041–1068 (2018)
7. A. Li, S. Singh, D. Sievenpiper, Metasurfaces and their applications. Nanophotonics **7**(6), 989–1011 (2018)
8. C.U. Hail, A.K.U. Michel, D. Poulikakos, H. Eghlidi, Optical metasurfaces: evolving from passive to adaptive. Adv. Opt. Mater. **7**(14), 1801786 (2019)
9. X. Li, X. Ma, X. Luo, Principles and applications of metasurfaces with phase modulation. Opto-Electronic Engineering **44**(3), 255–275 (2017)
10. V.C. Su, C.H. Chu, G. Sun, D.P. Tsai, Advances in optical metasurfaces: fabrication and applications. Opt. Express **26**, 13148–13182 (2018)
11. Y. Hu, X. Wang, X. Luo, X. Ou, L. Li, Y. Chen, P. Yang, S. Wang, H. Duan, All-dielectric metasurfaces for polarization manipulation: principles and emerging applications. Nanophotonics **9**(12), 3755–3780 (2020)
12. W. Wang, Z. Guo, K. Zhou, Y. Sun, F. Shen, Y. Li, S. Qu, S. Liu, Polarization-independent longitudinal multi-focusing metalens. Opt. Express **23**(23), 29855–29866 (2015)
13. L. Luo, Y. Zou, C. Ge, K. Zheng, D. Wang, R. Lu, T. Zhang, Y. Yu, Z. Guo, A surface plasmon enhanced near-infrared nanophotodetector. Adv. Opt. Mater. **4**(5), 763–771 (2016)

14. L. Luo, K. Wang, K. Guo, F. Shen, X. Zhang, Z. Yin, Z. Guo, Tunable manipulation of terahertz wavefront based on graphene metasurfaces. J. Opt. **19**(11), 115104 (2017)
15. N. Yu, P. Genevet, M.A. Kats, F. Aieta, J.P. Tetienne, F. Capasso, Z. Gaburro, Light propagation with phase discontinuities: generalized laws of reflection and refraction. Science **334**(6054), 333–337 (2011)
16. K. Guo, C. Wang, Q. Kang, L. Chen, Z. Guo, Broadband achromatic metalens with polarization insensitivity in the mid-infrared range. Opt. Mater. **131**, 112489 (2022)
17. Q. Kang, D. Li, K. Guo, J. Gao, Z. Guo, Tunable thermal camouflage based on GST plasmonic metamaterial. Nanomaterials **11**(2), 260 (2021)
18. K. Guo, X. Li, H. Ai, X. Ding, L. Wang, W. Wang, Z. Guo, Tunable oriented mid-infrared wave based on metasurface with phase change material of GST. Res. Phys. **34**, 105269 (2022)
19. H. Zhou, L. Chen, F. Shen, K. Guo, Z. Guo, Broadband achromatic metalens in the midinfrared range. Phys. Rev. Appl. **11**(2), 024066 (2019)
20. Y. Yao, R. Shankar, M.A. Kats, Y. Song, J. Kong, M. Loncar, F. Capasso, Electrically tunable metasurface perfect absorbers for ultrathin midinfrared optical modulators. Nano Lett. **14**(11), 6526–6532 (2014)
21. C. Wu, Y. Fang, L. Luo, K. Guo, Z. Guo, A dynamically tunable and wide-angle terahertz absorber based on graphene-dielectric grating. Mod. Phys. Lett. B **34**(27), 2050292 (2020)
22. P. Genevet, F. Capasso, Holographic optical metasurfaces:a review of current progress. Rep. Prog. Phys. **78**(2), 024401 (2015)
23. L. Li, T.J. Cui, W. Ji, S. Liu, J. Ding, X. Wan, Y.B. Li, M. Jiang, C.W. Qiu, S. Zhang, Electromagnetic reprogrammable coding metasurface holograms. Nat. Commun. **8**(1), 024401 (2017)
24. G. Zheng, N. Zhou, L. Deng, G. Li, J. Tao, Z. Li, Full-space metasurface holograms in the visible range. Opt. Express **29**(2), 2920–2930 (2021)
25. B. Xiong, L. Deng, R. Peng, Y. Liu, Controlling the degrees of freedom in metasurface designs for multi-functional optical devices. Nanoscale. Adv. **1**(10), 3786–3806 (2019)
26. S. Boroviks, R.A. Deshpande, N.A. Mortensen, S.I. Bozhevolnyi, Multifunctional metamirror: Polarization splitting and focusing. ACS Photonics **5**(5), 1648–1653 (2017)
27. Q. Kang, D. Li, W. Wang, K. Guo, Z. Guo, Multiband tunable thermal camouflage compatible with laser camouflage based on GST plasmonic metamaterial. J. Phys. D Appl. Phys. **55**(6), 065103 (2021)
28. B. Zhang, Z. Li, Z. Hu, J. Zhang, J. Wang, Analysis of a bidirectional metamaterial perfect absorber with band-switchability for multifunctional optical applications. Results in Physics **34**, 105313 (2022)
29. J. Yang, X. Wu, J. Song, C. Huang, Y. Huang, X. Luo, Cascaded metasurface for simultaneous control of transmission and reflection. Opt. Express **27**(6), 9061–9070 (2019)
30. T. Cai, G.M. Wang, S.W. Tang, H.X. Xu, J.W. Duan, H.J. Guo, F.X. Guan, S.L. Sun, Q. He, L. Zhou, High-efficiency and full-space manipulation of electromagnetic wave-fronts with metasurfaces. Phys. Rev. Appl. **8**(3), 034033 (2017)
31. R.Y. Wu, L. Zhang, L. Bao, L.W. Wu, Q. Ma, G.D. Bai, H.T. Wu, T.J. Cui, Digital metasurface with phase code and reflection-transmission amplitude code for flexible full-space electromagnetic manipulations. Adv. Opt. Mater. **7**(8), 1801429 (2019)
32. L. Deng, Z. Li, Z. Zhou, Z. He, Y. Zeng, G. Zheng, S. Yu, Bilayer-metasurface design, fabrication, and functionalization for full-space light manipulation. Adv. Opt. Mater. **10**(7), 2102179 (2022)
33. S. Zhao, J. Zhou, Z. Hu, J. Wu, J. Wang, Halogen-perovskite metasurfaces for trichromatic channel color holographic imaging. Opt. Express **29**(26), 43316–43326 (2021)
34. K. Cheng, Z. Hu, Y. Wang, J. Ma, J. Wang, High-performance terahertz vortex beam generator based on square-split-ring metasurfaces. Opt. Lett. **45**(21), 6054–6057 (2020)
35. K. Rouhi, H. Rajabalipanah, A. Abdolali, Real-time and broadband terahertz wave scattering manipulation via polarization-insensitive conformal graphene-based coding metasurfaces. Ann. Phys. **530**(4), 1700310 (2018)
36. N.A. Butakov, I. Valmianski, T. Lewi, C. Urban, Z. Ren, A.A. Mikhailovsky, S.D. Wilson, I.K. Schuller, J.A. Schuller, Switchable plasmonic-dielectric resonators with metal-insulator transitions. ACS Photonics **5**(2), 371–377 (2017)
37. K. Thyagarajan, R. Sokhoyan, L. Zornberg, H.A. Atwater, Millivolt modulation of plasmonic metasurface optical response via ionic conductance. Adv. Mater. **29**(31), 1701044 (2017)
38. A.S. Barker, H.W. Verleur, H.J. Guggenheim, Infrared optical properties of vanadium dioxide above and below the transition temperature. Phys. Rev. Lett. **17**(26), 1286–1289 (1966)
39. P. Kepic, F. Ligmajer, M. Hrton, H. Ren, L.D. Menezes, S.A. Maier, T. Sikola, Optically tunable Mie resonance VO_2 nano-antennas for metasurfaces in the visible. ACS Photonics **8**(4), 1048–1057 (2021)
40. R. Yahiaoui, Z.A. Chase, C. Kyaw, E. Seabron, J. Mathews, T.A. Searles, Dynamically tunable single-layer VO_2/metasurface based THz cross-polarization converter. J. Phys. D: Appl. Phys. **54**(23), 235101 (2021)
41. R. Kargar, K. Rouhi, A. Abdolali, Reprogrammable multifocal THz metalens based on metal-insulator transition of VO_2-assisted digital metasurface. Opt. Commun. **462**, 125331 (2020)
42. T. Wang, J. He, J. Guo, X. Wang, S. Feng, F. Kuhl, M. Becker, A. Polity, P. Klar, Y. Zhang, Thermally switchable terahertz wavefront metasurface modulators based on the insulator-to-metal transition of vanadium dioxide. Opt. Express **27**(15), 20347–20357 (2019)
43. J. He, Z. Xie, W. Sun, X. Wang, Y. Ji, S. Wang, Y. Lin, Y. Zhang, Terahertz tunable metasurface lens based on vanadium dioxide phase transition. Plasmonics **11**, 1285–1290 (2016)
44. F. Ding, S. Zhong, S.I. Bozhevolnyi, Vanadium dioxide integrated metasurfaces with switchable functionalities at terahertz frequencies. Adv. Opt. Mater. **6**(9), 1701204 (2018)
45. W. Chen, R. Chen, Y. Zhou, R. Chen, Y. Ma, Spin-dependent switchable metasurfaces using phase change materials. Opt. Express **27**(18), 25678–25687 (2019)
46. L. Kang, Y. Wu, D.H. Werner, Active terahertz spin hall effect in vanadium dioxide metasurfaces. Opt. Express **29**(6), 8816–8823 (2021)
47. C. Wan, Z. Zhang, D. Woolf, C.M. Hessel, J. Rensberg, J.M. Hensley, Y. Xiao, A. Shahsafi, J. Salman, S. Richter, Y. Sun, M.M. Qazilbash, R. Schmidt-Grund, C. Ronning, S. Ramanathan, M.A. Kats, On the optical properties of thin-film vanadium dioxide from the visible to the far infrared. Ann. Phys. **531**, 1900188 (2019)
48. J. Rensberg, S. Zhang, Y. Zhou, A.S. McLeod, C. Schwarz, M. Goldflam, M. Liu, J. Kerbusch, R. Nawrodt, S. Ramanathan, D.N. Basov, F. Capasso, C. Ronning, M.A. Kats, Active optical metasurfaces based on defect engineered phase-transition materials. Nano Lett. **16**, 1050 (2016)

49. J. Rensberg et al., Active optical metasurfaces based on defect-engineered phase-transition materials. Nano Lett. **16**(2), 1050–1055 (2016)
50. P.U. Jepsen, B.M. Fischer, A. Thoman, H. Helm, J.Y. Suh, R. Lopez, R.F. Haglund, Metal-insulator phase transition in a VO_2 thin film observed with terahertz spectroscopy. Phys. Rev. B **74**, 205103 (2006)
51. F. Ding, Y. Yang, R.A. Deshpande, S.I. Bozhevolnyi, A review of gap-surface plasmon metasurfaces: fundamentals and applications. Nanophotonics. **7**(6), 1129–1156 (2018)
52. N.K. Grady, J.E. Heyes, D.R. Chowdhury, Y. Zeng, M.T. Reiten, A.K. Azad, A.J. Taylor, D.A. Dalvit, H.T. Chen, Terahertz metamaterials for linear polarization conversion and anomalous refraction. Science **340**(6138), 1304–1307 (2013)